



# Topography of the 410 and 660 km discontinuities beneath the Tibetan plateau and adjacent areas

Zexin Miao<sup>a</sup>, Stephen S. Gao<sup>a</sup>, Muchen Sun<sup>b</sup>, Kelly H. Liu<sup>a,\*</sup>

<sup>a</sup> Department of Earth Sciences and Engineering, Missouri University of Science and Technology, Rolla, MO, USA

<sup>b</sup> Department of Geological Engineering, Montana Technological University, Butte, MT, USA

## ARTICLE INFO

### Keywords:

Tibetan Plateau  
Mantle transition zone  
Receiver function analysis  
Slab subduction  
Slab dehydration  
Tengchong volcanic field

## ABSTRACT

To investigate the three-dimensional spatial distribution of subducted oceanic slab segments and their consequential effect on the thermal and hydrous composition of the mantle transition zone (MTZ) beneath the entire Tibetan Plateau, we conducted a comprehensive analysis of approximately 655,000 P-to-s receiver functions (RFs), obtained from 735 broadband seismic stations. These RFs were utilized to delineate the 410 km (d410) and 660 km (d660) seismic discontinuities, which represent the upper and lower boundaries of the MTZ, respectively. The RFs were grouped within circular bins with a radius of 1 degree and stacked to image the discontinuities. The mean apparent depths derived based on the 1-D IASP91 Earth model for the d410 and d660 across the entire study area are  $412.2 \pm 8.3$  km and  $668.9 \pm 8.5$  km respectively, and the MTZ thickness is  $256.5 \pm 6.9$  km. The observed apparent depths underwent subsequent correction utilizing multiple velocity models. Several areas in central Tibet exhibit a normal d410 and an anomalously deep d660, which can be attributed to the combined effect of the negative thermal anomaly and dehydration associated with subducted slab segments that have penetrated at least to the d660 depth. The anomalous thickening of the MTZ beneath the southeastern Tibetan Plateau surrounding the Tengchong volcanic field can be explained by the dehydration of the subducted Indian Slab. Significant thinning of the MTZ associated with the deepening of the d410 beneath the western Tian Shan may indicate active thermal upwelling originating from the MTZ.

## 1. Introduction

### 1.1. Geological history and tectonic setting of the study area

The Himalayas and the Tibetan Plateau (Fig. 1) represent the ongoing geotectonic aftermath of a continental collision initiated approximately 65 million years ago (Yin and Harrison, 2000; Ding et al., 2005). Preceding this collision, the Indian tectonic plate underwent a rapid northward drift covering around 6000 km over a time span of 20 Ma (Yin and Harrison, 2000), implying that several thousand kilometers of oceanic lithosphere have been subducted since the Late Cretaceous. The region of study comprises multiple tectonic terranes, including the Himalayan, Lhasa, Qiangtang, and Songpan-Ganzi. The Himalayan terrane, wedged between the Indian shield to the south and the Indus-Yalu suture to the north (Fig. 1), evolved from the mid-Proterozoic to the Cretaceous period (Yin and Harrison, 2000). The Himalayan orogenesis was instigated by the collision of the Indian and Eurasian plates. The Lhasa terrane, positioned between the Indus-Yalu

and the Bangong-Nujiang sutures (Fig. 1), collided with the Qiangtang terrane during the late Jurassic (Dewey et al., 1988). The compressive forces resultant from this collision persisted until the early Late Cretaceous, leading to a minimum internal north-south contraction of the terrane by 180 km (Murphy et al., 1997). The Qiangtang terrane, situated between the Jinsha suture to the north and the Bangong-Nujiang suture to the south, spans 500–600 km in central Tibet, tapering to less than 150 km in the western Kunlun and eastern Tibet. During the Late Triassic, crustal thickening was concurrent with the southward subduction of the Songpan-Ganzi terrane underneath the Qiangtang terrane, leading to the formation of a detachment fault in central Qiangtang (Yin and Harrison, 2000).

The distribution of intraplate volcanoes in western China and surrounding areas is concentrated along the southeastern and northwestern edges of the Tibetan Plateau, particularly in the Tengchong region of Yunnan Province and the Kunlun Volcanic Group (Fig. 1). In southeastern Tibet, the Indian Plate undergoes an oblique subduction eastward beneath Burma, resulting in active seismicity that extends to

\* Corresponding author.

E-mail address: [liukh@mst.edu](mailto:liukh@mst.edu) (K.H. Liu).

<https://doi.org/10.1016/j.epsl.2024.118947>

Received 10 December 2023; Received in revised form 8 August 2024; Accepted 10 August 2024

Available online 21 August 2024

0012-821X/© 2024 Elsevier B.V. All rights are reserved, including those for text and data mining, AI training, and similar technologies.

depths of around 200 km (Xu et al., 2018). Despite extensive studies conducted to elucidate the origin of volcanic activity in the Tengchong area (Yang et al., 2019; Zou et al., 2017; Lei et al., 2019), the underlying processes responsible for their formation remain puzzling. Zou et al. (2017) suggest that the Tengchong volcano may have arisen due to the subduction of the Indian continental lithosphere, while others (e.g., Lei et al., 2019) attribute it to the wet and hot upwelling caused by dehydration of the subducted Indian slab. Another significant volcanic field in the study area, the Kunlun Volcanic Group, is situated in the northwestern Tibet. The Kunlun Range shows evidence of continental breakup and ocean development during the Neoproterozoic, followed by subduction and continental collisions, as well as intracontinental

extension and contractional deformation (Wu et al., 2019). The northward subduction of the Indian Plate underthrusts the entire plateau to this northwestern margin (Wei et al., 2015). The volcanoes have a rich geological history influenced by major arc activities during different periods and are closely associated with the faults in the area (Xu et al., 2021).

1.2. Results from previous seismic tomography and receiver function investigations

To elucidate the spatial heterogeneity of subducted slab segments, their inherent physical characteristics, and their consequential impacts

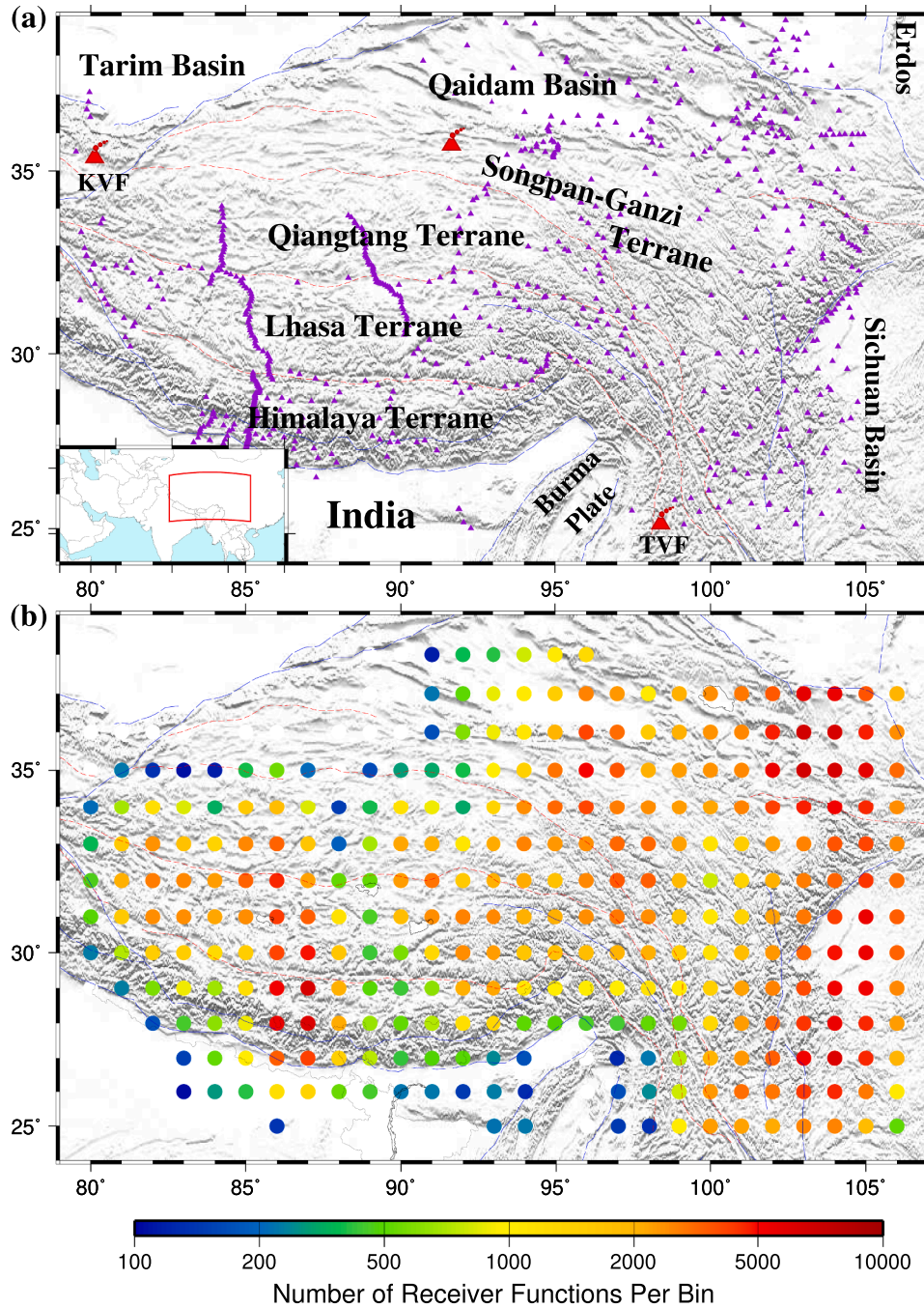


Fig. 1. (a) Topographic relief map of the study area showing major tectonic boundaries and the distribution of seismic stations (purple triangles) used in the study. The blue and red dashed lines respectively indicate the major faults and major suture zones in the study area, respectively. The red triangles represent Cenozoic volcanoes. KVF: Kunlun Volcanic Field; TVF: Tengchong Volcanic Field. (b) Number of receiver functions per bin.

on mantle dynamics and geohazards, various studies leveraging seismic tomography and receiver function methodologies have been implemented within the Tibetan Plateau and its peripheries (e.g., Nie et al., 2020; Feng et al., 2020; Li et al., 2008; Liu et al., 2017; Li and Song, 2018; Li and van der Hilst, 2010; Wei and Zhao, 2020; Zhang et al., 2018).

1.2.1. Seismic tomography results

Most tomographic images of the upper mantle beneath the Tibetan Plateau reveal a band of high-velocity anomalies, ascribed to the

subducted Indian Plate which is presumably colder than the ambient mantle. However, notable disparities persist among previous studies regarding the depth range, geometric configuration, and spatial distribution of the subducted lithospheric fragments in the region (Fig. 2). Certain investigations center on the upper mantle domain and propose that elevated-velocity anomalies manifest distinctly above the d410 (Liang et al., 2016a, Zhao et al., 2014, Zhang et al., 2015), while others suggest that they extend to the lower MTZ above the d660 (Zhang et al., 2018; Wei and Zhan, 2020; Li et al., 2008; Replumaz et al., 2013) or lower mantle beneath the d660 (Lei and Zhao, 2016; Huang et al., 2015;

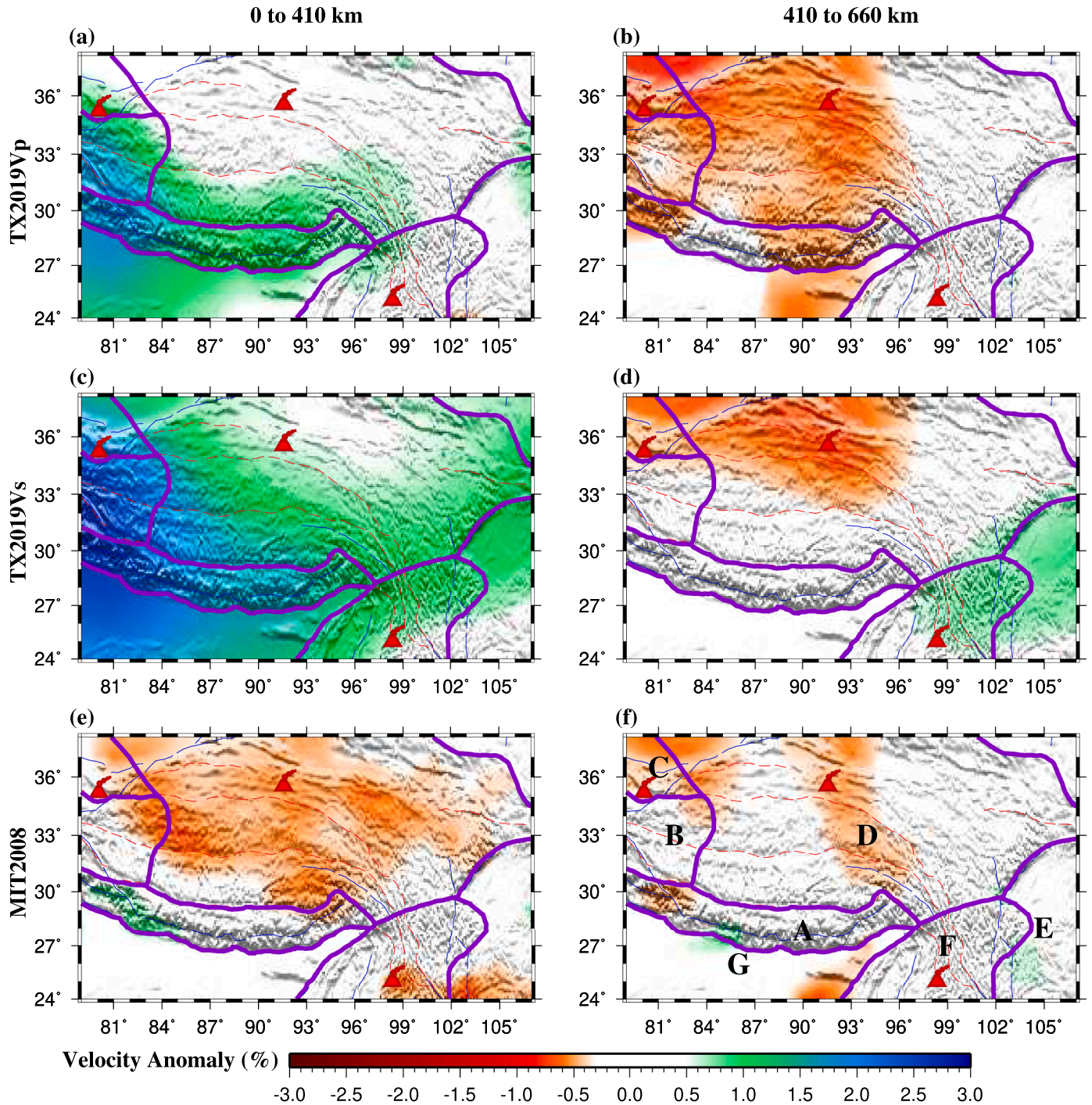


Fig. 2. Averaged upper mantle (0–410 km; left column) and MTZ (410–660 km; right column) seismic wave velocity anomalies from previous studies. MIT2008 is from Li et al. (2008), and both TX2019Vs and TX2019Vp are from Lu et al. (2019). The purple lines mark the seven regions with similar characteristics in the resulting discontinuity depths. A: Himalayan Orogen; B: Western Himalaya; C: NW Tibetan Plateau; D: Central Tibet; E: Western Yantze Craton; F: Southeast Tibet; G: Northern Indian Craton.

Li and van der Hilst, 2010). Furthermore, the resultant velocity anomalies are significantly variable among prior studies, particularly concerning the MTZ and the upper-most lower mantle where the vertical resolution diminishes significantly. While some studies suggest a generally lower than normal upper mantle velocity (Li and van der Hilst, 2010), a recent global scale study (Lu et al., 2019) reveals normal or higher than normal mean upper mantle P- and S-wave velocities (Fig. 2).

Seismic tomographic images produced by Li and Song (2018) show regions of high velocities separated by low-velocity bands, suggesting that the fragmentation of the Indian mantle lithosphere may explain the rifting that occurred during the Late Miocene and Quaternary, as well as the crustal deformation and intermediate-depth seismic activity in the southern and central territories of the Tibetan Plateau. This also implies a robust interconnection between crustal and mantle lithospheric deformations (Li and Song, 2018). The Indian Plate is believed to be segmented by north-south faults that facilitate or encourage upwellings of the asthenosphere (Liang et al., 2016a).

Within the Tengchong region located in the southeastern Tibetan Plateau, although some previous studies suggest that intraplate volcanism in Tengchong bears a substantial correlation with slab subduction, there remains a debate regarding the origination depth of the magma (Yang et al., 2019; Zou et al., 2017; Lei et al., 2019). For instance, several teleseismic tomography investigations propose that the thermal anomalies associated with the Tengchong volcano may extend to the depth of the MTZ (Lei et al., 2009, 2019; Huang et al., 2015), while alternative tomographic models have unveiled widespread low-velocity anomalies in the shallow mantle (Li et al., 2008; Wei et al., 2012). More recent studies (e.g., Wei and Zhao, 2020) suggest that the Tengchong volcanism may be associated with the subduction of the Burma slab and regional lithospheric extension of the Eurasian lithosphere.

The Kunlun Volcanic Group located on the western Tibetan Plateau has been less extensively studied compared to other regions like Tengchong, primarily due to sparse seismic data availability. Despite this, seismic studies have revealed some intriguing crust and mantle features beneath this region (e.g., Liang et al., 2016). High velocity anomalies demonstrate a clear dipping geometry that extends down to the MTZ, with variations observed along the Himalayan arc in the south. This pattern likely signifies the subduction of the Indian slab reaching the MTZ beneath the area. Additionally, low-velocity anomalies detected in the uppermost mantle, and possibly extending to the transition zone beneath the Kunlun volcanic fields and adjacent regions, suggest hot and wet mantle upwelling, a process typically driven by subduction. These volcanic activities may be linked to the subduction of nearby Indian Plate and regional lithospheric extensions, suggesting complex geological processes at depth that drive the surface volcanism observed in the Kunlun area.

### 1.2.2. Results from previous receiver function imaging of the MTZ discontinuities

The mineralogical phase transitions of olivine to wadsleyite and ringwoodite to bridgmanite are denoted by discontinuities at the proximate depths of 410 km and 660 km, respectively (Ringwood, 1975). The phase transition at the d410 exhibits a positive Clapeyron slope, whereas the transition at the d660 demonstrates a negative Clapeyron slope (Bina and Helffrich, 1994). As such, if a positive thermal anomaly correlates with mantle upwelling penetrating the MTZ, it would induce a depression of the d410 and an uplift of the d660, consequently leading to a reduction in MTZ thickness. In contrast, negative thermal anomalies, such as those related to cold subducting slabs or lithospheric downwelling, would result in MTZ thickening. Beyond thermal conditions of 1800°C, the phase transition at the d660 is characterized by a positive Clapeyron slope, primarily governed by the transition from majorite garnet to perovskite (Hirose, 2002).

In addition to thermal variations, an abnormally elevated concentration of water within the MTZ may contribute to the undulation of MTZ discontinuities. Experimental investigations (Litasov et al., 2005;

Ohtani and Litasov, 2006; Smyth and Frost, 2002) suggest that an overabundance of hydrous minerals proximate to the MTZ can instigate an uplift of the d410 and a depression of the d660. Moreover, water can induce a less distinct d410 by increasing the depth range required for the phase transition to occur, resulting in a reduction in the amplitude but an increase in the breadth of the P410s arrival (Smyth and Frost, 2002).

In the study area, a majority of preceding receiver function analyses have primarily focused on either Central Tibet or Southeastern Tibet, and a comprehensive investigation of MTZ discontinuities across the entire Tibetan Plateau using recently available broadband seismic data is lacking. Underneath Central Tibet, an anomalously thickened MTZ is observed and is interpreted as indicative of a dislocated remnant lithosphere or a subducted slab within the MTZ (Duan et al., 2016, 2017; Liang et al., 2016b; Wu et al., 2022). A recent regional-scale examination of MTZ discontinuities in Southeastern Tibet was undertaken by Xu et al. (2018), which employed broadband seismic data recorded by 398 stations. The results presented a deeper d410, implying a warmer-than-normal MTZ and consequently supporting the hypothesis that the Tengchong volcano originates from the MTZ. Zhang et al. (2017) proposed a differing interpretation based on the depth variations of the MTZ discontinuities revealed by receiver functions, suggesting that the volcano may have been formed due to tearing of the Indian Plate in the upper mantle.

### 1.3. Rationale of the current study

Despite numerous observational and geodynamic modelling investigations, the configuration and depth range of subducted slab segments beneath the entire Tibetan Plateau remain contentious, predominantly due to the facts that 1) virtually all MTZ imaging studies utilizing recently-available broadband seismic data dealt with small portions of the Tibetan Plateau, and 2) the resolution of seismic tomography methodologies reduces significantly at increased depths (Dong et al., 2019; Nie et al., 2020; Zhang et al., 2020). This investigation intends to image the topography of the MTZ discontinuities underneath the Tibetan Plateau and its neighboring regions, capitalizing on an over 5-fold increment in the quantity of broadband seismic stations compared to the most recent MTZ study utilizing receiver functions (Duan et al., 2016, 2017; Xu et al., 2018; Zhang et al., 2017). The resulting discontinuity depths and the thickness of the MTZ across the entire Tibetan Plateau provide new insights into the spatial distribution of subducted slab segments in the MTZ, and thermal and water content anomalies in the MTZ.

## 2. Data and methods

### 2.1. Data and receiver function calculation

The study utilized available broadband passive seismic data acquired from the Seismological Facility for the Advancement of Geoscience (SAGE) Data Management Center, and the Data Management Centre of China National Seismic Network at the Institute of Geophysics, China Earthquake Administration. The selection criteria for the seismic data set were established based on two factors: (1) the epicentral distances ranged between 30° and 100°, and (2) the cutoff magnitude ( $M_c$ ) was determined by the epicentral distance ( $\Delta$ ) and focal depth ( $D$ ), according to an empirical equation  $M_c = Mw_{min} + \frac{(\Delta - \Delta_{min})}{(180.0 - \Delta_{min})} - \frac{D}{D_{max}}$ , where  $Mw_{min} = 5.2$ ,  $\Delta_{min} = 30^\circ$  and  $D_{max} = 700$  km (Liu and Gao, 2010). This equation aims at maintaining a balance between the quantity and quality of the seismic data to be requested from the data centers, and has been utilized in several studies (e.g., Dahm et al., 2017; Gao and Liu, 2014b; Sun et al., 2018, 2020; Yu et al., 2017). The methodology and parameters employed for data processing in this investigation are the same as those employed in Gao and Liu (2014a, 2014b) and are summarized as follows. In order to increase the signal-to-noise ratio (SNR) of the

seismograms, a two-pass, four-pole bandpass Bessel filter with corner frequencies of 0.02 and 0.2 Hz was implemented. Two procedures based on SNR were executed to select high quality RFs. Seismograms possessing a P-wave SNR on the vertical component lower than 4.0 were excluded (Gao and Liu, 2014a). The SNR was determined as the maximal absolute amplitude on the vertical component within the time window of 8 s preceding and 12 s succeeding the estimated onset time of the initial P-wave, based on the IASP91 Earth model, divided by the mean absolute amplitude of the waveform 10-20 s before the theoretical P-wave onset (Gao and Liu, 2014a). Radial RFs in this investigation were computed utilizing a frequency-domain deconvolution method with a water level of 0.03 (Ammon, 1991; Clayton and Wiggins, 1976). The temporal window employed for the RF computation was 20 s prior to and 260 s post the initial P-arrival. To mitigate the impacts of potent PP arrivals on the resulting RFs, exponential weighting functions with a half-width of 30 s were applied to the seismograms prior to the RF computation (Gao and Liu, 2014a). A total of 655,026 high-quality RFs from 9121 events (Fig. 3) recorded by 735 stations (Fig. 1) were utilized in this investigation.

## 2.2. Moveout Correction and Stacking

To amplify the small amplitude of P-to-s converted waves from the MTZ discontinuities, it is often necessary to stack RFs from multiple station-event pairs in neighboring regions. Preceding stacking, the RFs are categorized into circular bins with a radius of 1 degree, computed on the theoretical coordinates of the P-to-s converted phase (Pds) at 535 km which is the middle of the MTZ, with adjacent bin centers partitioned by 1 geographic degree. A test performed by Sun et al. (2020) suggested that grouping the RFs separately at 410 and 660 km depths results in a slight change of MTZ thickness of less than 2 km. While some previous studies re-group the RFs at each depth (e.g., Dueker and Sheehan, 1997), as detailed in Dahm et al. (2017), grouping them at a single depth can

reduce the influence of strong upper mantle velocity heterogeneities on the resulting MTZ thickness. The RFs are corrected for moveout utilizing the IASP91 Earth model with a non-plane wavefront assumption and are subsequently stacked to generate depth series that span from 0 to 800 km with a vertical interval of 1 km, given that there are a minimum of four RFs in a bin (Gao and Liu, 2014a). The number of RF traces contributing to the stacking ranges from 4 to 7,082 per bin.

A bootstrapping methodology with 50 iterations, as delineated by Efron and Tibshirani (1986) and Liu et al. (2003) for applications in an MTZ study, was employed to compute the mean and standard deviation of the depths of MTZ discontinuities and the MTZ thickness for each bin. The depths of the d410 and d660 were determined for each bootstrap iteration by selecting the maximal stacking amplitude within a predetermined depth window, spanning from 380 to 440 km for the d410 and from 630 to 690 km for the d660, on the resultant depth series. The depths were subsequently visually scrutinized, and the predetermined depth window was modified as required for windows with multiple arrivals with similar strength. In this case the depth of the chosen peak is comparable with neighboring bins. The Pds phase from the d410 and d660 was generally well-resolved across the majority of the time series (Fig. 4, S1 and S2). Results from a small portion of the bins, mostly in the peripheral regions of the study area, may not be well constrained due to a low number of RFs (Fig. 1b). Resulting depth series from all the 14 E-W cross-sections can be found in Fig. S1, and those along the 27 N-S cross-sections can be found in Fig. S2. Assuming that the P-to-s converted phase has a dominant frequency of 0.2 Hz, the radius of the first Fresnel zone is about 78 km. Given that the radius of the circular bins is 1 degree (approximately 112 km), it suggests that a given bin samples an area with a radius of about 190 km. This gives an estimation of the spatial resolution of the results.

## 3. Results

### 3.1. Apparent depths

A total of 422 circular bins presents either discernible d410 or d660, within which 412 bins exhibit clear d410 arrivals and 407 bins feature distinct d660 arrivals, and 398 bins possess both (Table S1). Because the moveout correction was performed based on the 1-D IASP91 Earth model, the resultant depths are termed apparent depths which can be converted into “true” depths using various velocity models as described in the next section. Across the entire region, the average apparent depth is  $412.2 \pm 8.3$  km for the d410 and  $668.9 \pm 8.5$  km for the d660, with the average MTZ thickness being  $256.5 \pm 6.9$  km. The apparent depths demonstrate systematic spatial variations (Fig. 5). Taking into account the attributes of the depths of the observed discontinuities and the thickness of the MTZ, we divide the study area into seven distinct regions (Figs. 2 and 5, and Table 1). Within the Himalayan Orogen (Region A), the d410 displays an apparent uplift, and the d660 registers a normal value of about 660 km. An apparent uplift of approximately 7 km of the d410 was revealed in the westmost region of the Tibetan Plateau (Region B), and the d660 shows a standard value, resulting in a 7 km thickening of the MTZ. Note that for this area, the standard deviation (SD) is about 9 km for the d410 depths, which is the largest among all areas (Table 1). This large SD value is mostly caused by the fact that the d410 depth for the bin located at the boundary between Areas B and D is anomalously large (432 km). Excluding this bin, the SD reduces to about 5 km and the mean d410 depth becomes 402 km. The d410 observed in the NW Tibetan Plateau (Region C) is approximately 8 km deeper than the standard depth, and the d660 is marginally shallower than the standard depth. Beneath the main portion of the Tibetan Plateau (Region D), the d410 is about 5 km deeper and the d660 is 12 km deeper than their standard values, leading to an MTZ approximately 7 km thicker than normal on average. Beneath the Western Yangtze Craton (Region E), the average apparent depth is  $408.1 \pm 2.9$  km for the d410,  $662.9 \pm 4.0$  km for the d660, and the MTZ thickness is  $254.4 \pm 4.2$  km. The values for

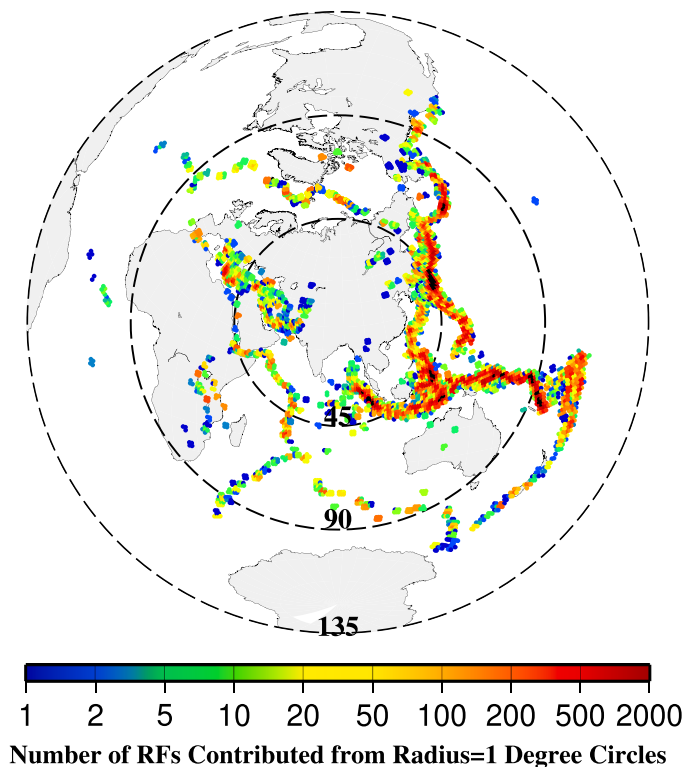
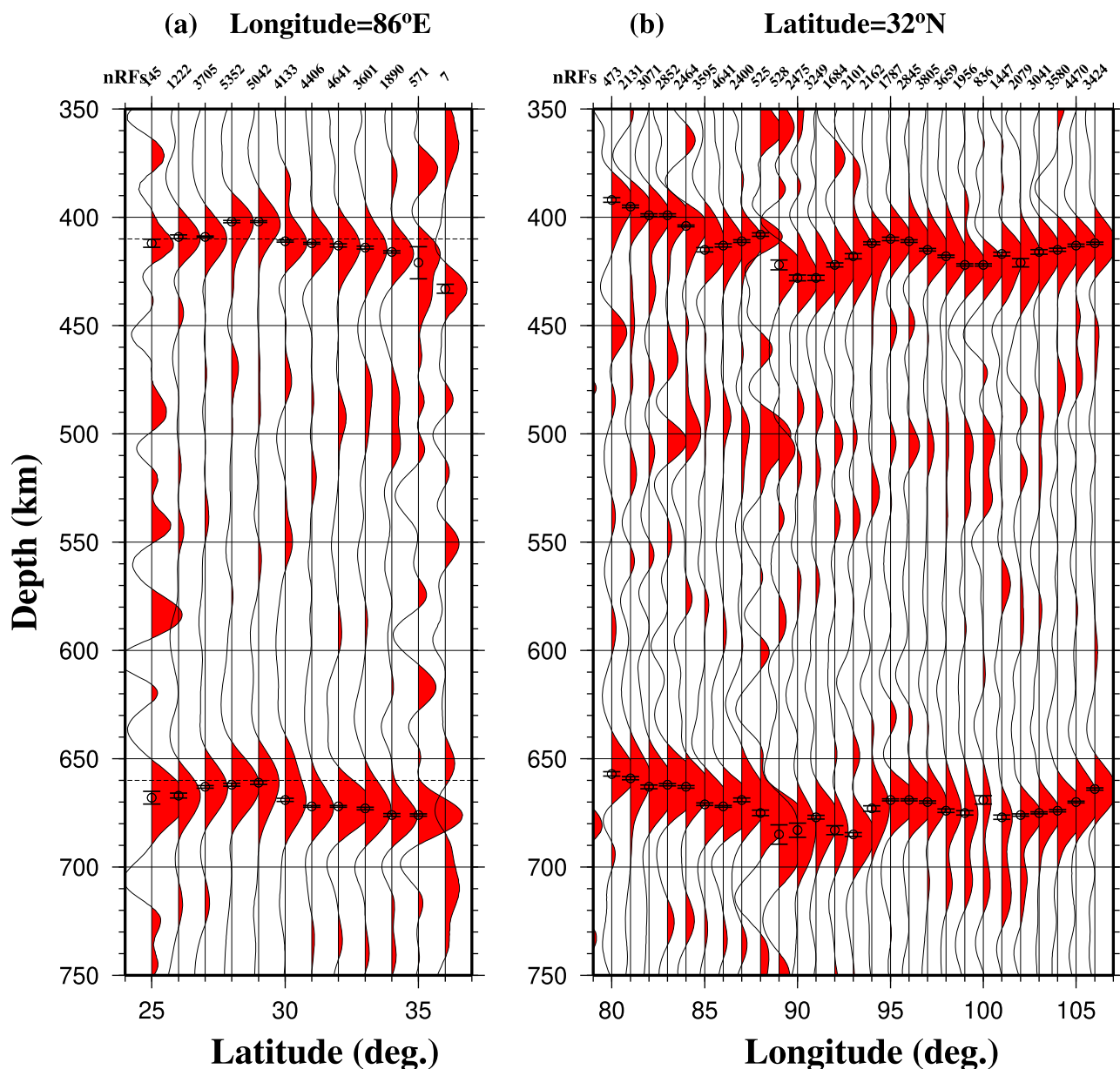


Fig. 3. An azimuthal equidistant projection map centered at the study area, showing the distribution of earthquakes utilized in the study. Each colored dot on the map represents the number of receiver functions employed from the earthquakes in that circle, with a radius of 1°.



**Fig. 4.** Depth series from stacking of RFs in radius = 1° bins along the (a) 86°E and (b) 32°N profiles. The average depths of the d410 and d660 obtained through bootstrap resampling are indicated by the circles, while the error bars represent two standard deviations of the depths. The number of RFs utilized in each bin is shown at the top of each trace.

SE Tibet (Region F) are  $414.2 \pm 5.9$  km for the d410,  $675.2 \pm 10.5$  km for the d660, and  $260.4 \pm 10.4$  km for MTZ thickness. For the Indian Craton (Region G), these values are  $408.9 \pm 5.7$  km for the d410,  $663.4 \pm 8.3$  km for the d660, and  $254.6 \pm 6.5$  km for MTZ thickness.

Fig. 5 illustrates the MTZ discontinuity depths and MTZ thickness calculated using the algorithm of continuous curvature surface gridding, with a predetermined tension factor of 0.5 (Smith and Wessel, 1990). Because the apparent depths were obtained utilizing the one-dimensional IASP91 Earth model, they are subject to several variables, including thermal anomalies and the existence of hydrated minerals within the MTZ, and velocity anomalies located above the discontinuities (see Mohamed et al., 2014 for a quantitative analysis of the influence of each of the factors on the observed apparent depths). The velocity anomalies existing within the crust and upper mantle significantly impact the apparent depths of both the d410 and d660, and their influence is largely correlated. Consequently, if the true depths of the d410 and d660 remain uniform across the examination area, a high

cross-correlation coefficient (XCC) between the apparent depths is anticipated. Additionally, high velocity anomalies in the crust and upper mantle result in an apparent elevation of both the d410 and d660, while low velocity anomalies induce an apparent lowering of both discontinuities. A high XCC between the depths of d410 and d660 could also be a reflection of the presence of considerable positive thermal anomalies proximal to the discontinuities, with temperatures surpassing 1800°C in the vicinity of d660. This leads to a positive Clapeyron slope for both d410 (Bina and Helffrich, 1994) and d660 (Hirose, 2002), thereby resulting in a positive XCC. However, this interpretation may not be applicable to the area of study, which is primarily characterized by subduction of cold slab segments.

The XCC between the observed apparent d410 and d660 depths in the study region is quantified as 0.65 (Fig. 5d). This value is relatively moderate when compared with the contiguous United States, which has an XCC of 0.84 (Gao and Liu, 2014b), and the Arabian Plate along with its adjacent areas with an XCC of 0.81 (Mohamed et al., 2014). This

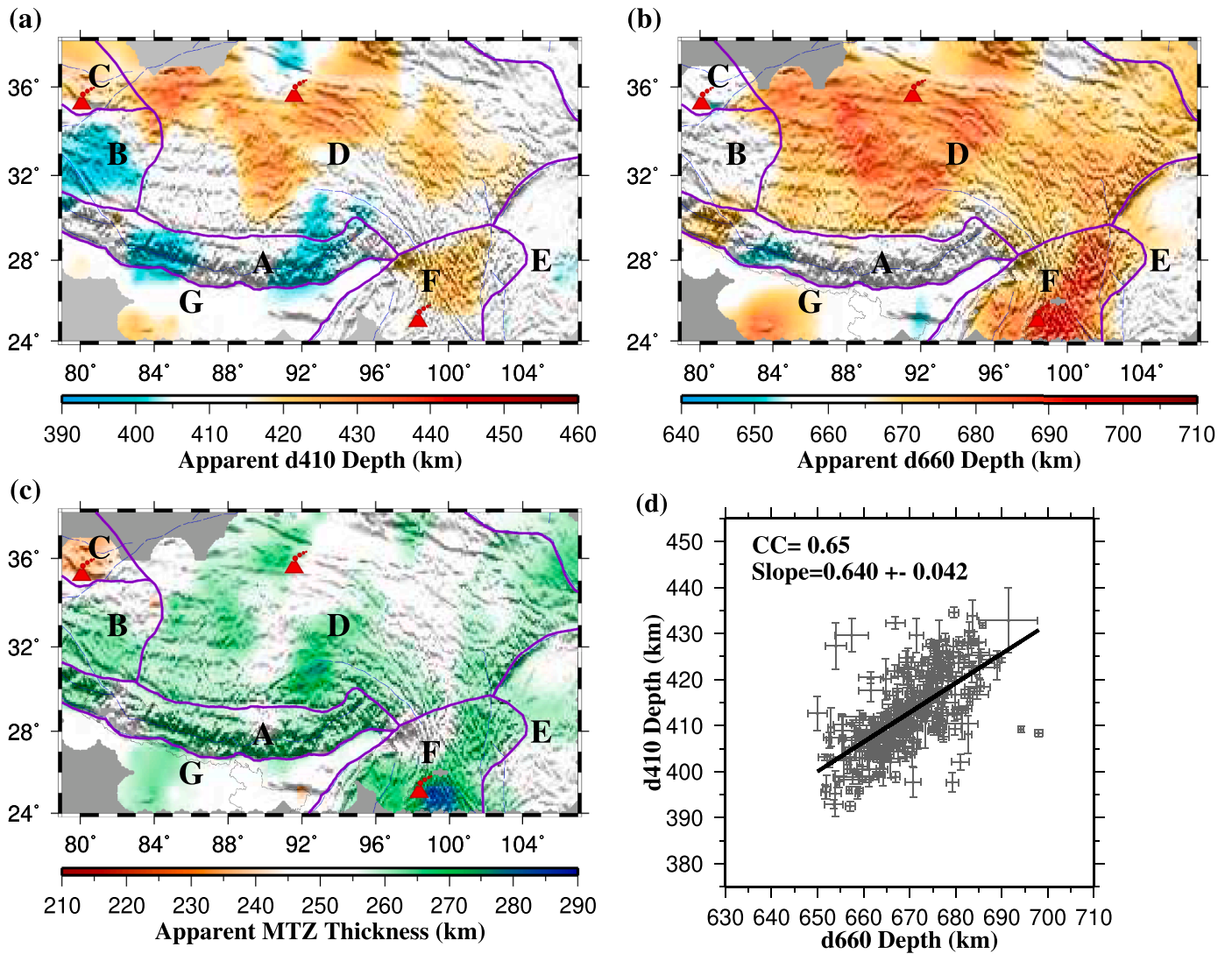


Fig. 5. (a) Spatial distribution of apparent d410 depth measurements obtained using the 1-D IASP91 Earth model. (b) Same as Fig. 5a but for the d660. (c) Apparent MTZ thicknesses. (d) Apparent depths of the d410 plotted with respect to the apparent d660 depths. CC: correlation coefficient.

**Table 1**  
Mean apparent measurements for the seven sub-regions

region	d410±σd410 (km)	d660±σd660 (km)	MTZ±σMTZ (km)	N. bins Name
Total	412.2±8.3	668.9±8.5	256.5±6.9	341
A	403.9±5.3	661.1±5.5	256.6±4.0	44 Himalayan orogen
B	403.3±8.9	660.6±4.0	257.0±7.5	18 W. Himalaya
C	418.1±7.1	659.7±9.9	242.8±13.8	11 NW Tibet
D	415.2±7.8	672.7±6.0	256.9±6.1	176 Central Tibet
E	408.1±2.9	662.9±4.0	254.4±4.2	24 W. Yangtze
F	414.2±5.9	675.2±10.5	260.4±10.4	34 SE Tibet
G	408.9±5.7	663.4±8.3	254.6±6.5	30 N. India

indicates that a significant proportion of the discerned spatial variation of the apparent depths within the research area can be attributed to thermal deviations, variations in water content, or velocity anomalies present within the MTZ, rather than velocity perturbations in the crust and upper mantle.

### 3.2. Velocity-corrected depths

In order to ascertain the "true" depths of the d410 and d660, global-

scale tomographic models were employed to correct the apparent depths using the approach as delineated in Gao and Liu (2014b). This study incorporated the P- and S-wave model of TX2019slab (Lu et al., 2019), along with the global P-wave models of MIT2008 (Li et al., 2008) and the P-wave portion of TX2019slab (herein referred to as TX2019Vp) to make velocity corrections. For the P-wave only models, the shear wave velocity anomaly was calculated utilizing the P-wave velocity anomaly and an optimal value of  $\gamma$ , defined by  $\gamma = \ln(V_s)/\ln(V_p)$ . This optimal value was procured through identification of the  $\gamma$  value that coincides with the minimal XCC between the corrected d410 and d660 depths (Gao and Liu, 2014b). The optimal  $\gamma$  values were found to be 1.75 for MIT2008 and 1.70 for TX2019Vp. The averaged measurements over results from the three velocity models are shown in Fig. 6, and results from each of the three models can be found in Figures S3-S5.

The XCC values between the corrected d410 and d660 depths amounted to 0.55 for MIT2008, 0.47 for TX2019Vp, and 0.56 for TX2019slab (Figures S3-S5). After velocity corrections utilizing MIT2008, TX2019Vp, and TX2019slab, the mean values of the resultant d410 depth, d660 depth, and MTZ thickness were (409.9±7.6 km, 666.5±8.0 km, 256.6±7.4 km), (418.7±7.2 km, 674.4±7.5 km, 255.7±7.6 km), and (420.4±9.4 km, 677.8±9.8 km, 257.5±10.2 km), respectively.

The mean resultant average corrected depths illustrate systematic spatial variations (Fig. 6). For the entire area, the average corrected

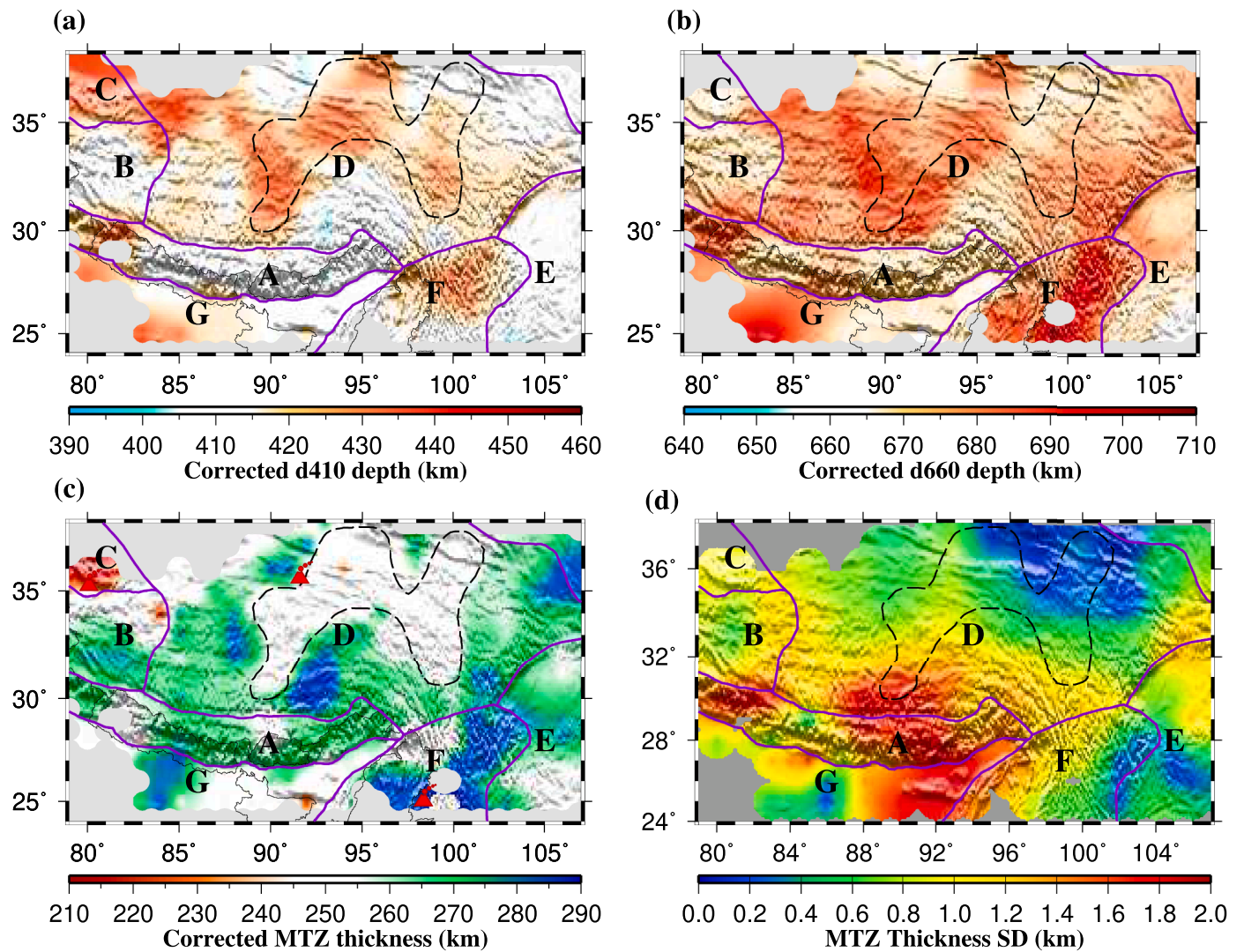


Fig. 6. (a) Average corrected depth of the d410 using velocity models MIT2008, TX2019Vp, and TX2019slab. (b) Same as Fig. 6a but for the d660. (c) Average thickness of MTZ. (d) Standard deviation of the mean MTZ thickness in km. The dashed outlines indicate an approximately semicircular area characterized by depressed d410 and d660 and a normal MTZ thickness.

depth measures  $416.3 \pm 8.1$  km for the d410 and  $672.9 \pm 8.4$  km for the d660, with an MTZ thickness of  $256.6 \pm 8.4$  km. In the Himalayan Orogen (Region A), the d410 depth adheres to normative values, whereas the d660 is 9 km deeper than the standard. The depression of approximately 10 km for the d660 is identified in the Western Himalaya (Region B), with the d410 depth slightly deeper than typical, culminating in a 6 km thickened MTZ. The corrected depth of d410 in the NW Tibetan Plateau (Region C) is approximately 15 km deeper than the normal depth, and the d660 depth exceeds the normal depth by 5 km, leading to a 10 km thinning of the MTZ. In Central Tibet (Region D), the d410 and d660 depths are about 7 km and 14 km deeper than their usual values, respectively, leading to an MTZ approximately 6 km thicker than normal. Beneath the Western Yangtze Craton (Region E), the mean depth measures  $410.5 \pm 4.2$  km for the d410,  $671.0 \pm 5.9$  km for the d660, with an MTZ thickness of  $257.2 \pm 4.3$  km. For SE Tibet (Region F), these values are  $417.7 \pm 6.3$  km for the d410,  $680.4 \pm 10.6$  km for the d660, and  $262.7 \pm 10.6$  km for the MTZ thickness, and for the northern Indian Craton (Region G), they measure  $416.8 \pm 6.3$  km for the d410,  $671.9 \pm 10.0$  km for the d660, and  $255.1 \pm 7.7$  km for the MTZ thickness.

## 4. Discussion

### 4.1. Dehydration of hydrous slab segments

Both the apparent depths (Fig. 5) and velocity-corrected results (Fig. 6) suggest an MTZ in the majority of the study area that exceeds typical thickness. This observation, when combined with the generally lower than normal mean velocities in the MTZ (Fig. 2), suggests that the MTZ thickening is likely attributed to a high concentration of water content within the MTZ rather than a lower than normal temperature. This is because subducted cold slab segments within the MTZ usually exhibit elevated seismic velocities, a phenomenon not concurrent with the lower-than-normal velocities observed in the MTZ from the majority of seismic tomography studies (Fig. 2). Mineralogical experiments have demonstrated that hydration of minerals such as wadsleyite and ringwoodite, found in the upper and lower MTZ respectively, can induce an uplift of the d410 and a depression of the d660 (Litasov et al., 2005). The maximum quantity of water that can be integrated into wadsleyite is around 3.3 wt.% (Inoue et al., 2010; Smyth, 1987), and for ringwoodite, the value is approximately 1.7 wt.% (Inoue et al., 2010). Litasov et al. (2005) suggested that the introduction of 2 wt.% of water into hydrous peridotite at a temperature of 1473 K can induce an uplift of 15–30 km

for the d410 and a depression of 15 km for the d660.

Along the eastern margin of the Tibetan Plateau and in the immediate eastern area, seismic tomography studies reveal normal velocities in the MTZ (Fig. 2), while the MTZ is significantly thickened (Fig. 6c). We speculate that these observations are due to the combination of low-temperature anomalies associated with subducted slab segments, which increase overall MTZ velocities and thickness, and water brought down by the subduction, which decreases overall MTZ velocities and also increases thickness (Ohtani and Litasov, 2006). The velocity and MTZ thickness observations in this area imply that temperature and water content anomalies contribute almost equally to the velocity anomalies, but with opposite signs, while both contribute positively to the thickening of the MTZ.

It is noteworthy to observe that while the depression of the d660 is pervasively observed in the main portion of the Tibetan Plateau (Area D in Fig. 6b), an approximate semicircular zone (the area outlined by the dashed lines in Fig. 6) shows a normal MTZ thickness. A comparison of the d410 depths (Fig. 6a) and the MTZ thickness (Fig. 6c) suggests that the d410, similar to the d660, is depressed, leading to a normal MTZ thickness. One of the possible causes for the depression of the d410 is a higher than normal temperature in the vicinity of the d410. However, the physical or chemical mechanisms instigating this thermal anomaly remain elusive. Alternatively, the fact that both the d410 and d660 depths are still deeper than normal and are approximately parallel to each other may suggest that the depths were inadequately corrected, probably due to the applied damping factor when the tomographic images were produced, or the removal of a regional mean velocity.

#### 4.2. Formation mechanism of intraplate volcanoes in SE Tibet

The MTZ beneath the eastern margin of the Tibetan Plateau (Area E and the eastern boundary area of Area D) shows greater than normal thickness (Fig. 6c). This thickening is mostly caused by the depression of the d660 (Fig. 6b), while the d410 remains at a normal to slightly greater than normal depth (Fig. 6a). Mineralogical experiments indicate that ancient ( $\geq 50$  Myr) and thermally diminished subducting slabs have the capacity to transport water into the MTZ, facilitated by hydrous minerals and dense hydrous magnesium silicates (Pearson et al., 2014; Thompson, 1992). Sustained and progressive dehydration of the subducted slab is enabled by a reduction in water solubility of wadsleyite and ringwoodite concurrent with increased temperature (Ohtani et al., 2004). The high concentration of water within the MTZ, combined with the prolonged ( $\sim 60$  million years) subduction history of the Indian Plate, supports the hypothesis linking the Tengchong volcanic activity to wet upwelling stemming from dehydration of the subducted Indian slab (Xu et al., 2018; Zhang et al., 2017).

#### 4.3. Thermal upwelling beneath the Kunlun volcanic group (Area C)

The MTZ thickness underneath the Kunlun Volcanic Group (Area C) in northwestern Tibet is noticeably reduced, demonstrating an average thinning of about 10 km in comparison to the typical MTZ thickness. This thinning is primarily focused on the vicinity of the Cenozoic Kunlun Volcanic Group and is associated with a 15 km depression of the d410 (Fig. 6a) and a 5 km depression of the d660 (Fig. 6b). A plausible hypothesis for the anomalously reduced MTZ thickness in this area involves the ascent of thermal anomalies from the upper MTZ to the surface. Based on the studies by Bina and Helffrich (1994) and Fei et al. (2004), assuming Clapeyron slopes of  $+2.9$  MPa/K for the d410 and  $-1.3$  MPa/K for the d660, the 10 km thinning of the MTZ corresponds to a thermal anomaly of 121 K within the MTZ. This thermal anomaly has been suggested from various studies employing different methodologies. For instance, geochemical assessments propose that the lithic compositions of the Kunlun Volcanic Group originate from the depleted mantle, devoid of subduction zone contamination (Zhang et al., 2003).

## 5. Conclusions

Using an unprecedented number of receiver functions recorded on the Tibetan Plateau and adjacent areas, we imaged the topography of the MTZ discontinuities with greatly improved spatial coverage and resolution over previous studies in the area. The results reveal pervasive depression of the d660 beneath most parts of the Tibetan Plateau. Combined with previously revealed lower-than-normal seismic velocities in the MTZ, this observation suggests the presence of an unusually high amount of hydrous minerals in the lower MTZ. In a semicircular area of the central Tibetan Plateau, both the d410 and d660 are deeper than normal, resulting in a normal MTZ thickness. The eastern margin of the Tibetan Plateau, including the Tengchong volcanic field, exhibits normal MTZ velocity anomalies and a thicker-than-normal MTZ, possibly caused by cold temperatures and high water content anomalies associated with subducted slab segments. The dehydration of these slab segments is attributable to the Cenozoic volcanism observed in the Tengchong area. In western Kunlun, a thinner-than-normal MTZ associated with the depression of the d410 is most likely caused by higher-than-normal temperatures in the upper MTZ that are possibly indicative of thermal upwelling with an origination from the upper MTZ.

#### CRediT authorship contribution statement

**Zexin Miao:** Writing – original draft, Visualization, Validation, Investigation, Formal analysis, Data curation. **Stephen S. Gao:** Writing – review & editing, Software, Methodology, Funding acquisition, Conceptualization. **Muchen Sun:** Writing – review & editing, Visualization, Formal analysis. **Kelly H. Liu:** Writing – review & editing, Supervision, Software, Resources, Project administration, Methodology, Funding acquisition, Data curation, Conceptualization.

#### Declaration of competing interest

The authors declare no conflicts of interest.

#### Data availability

Data will be made available on request.

#### Acknowledgements

We thank two anonymous reviewers and Editor Thybo for constructive reviews and comments that significantly improved the manuscript. Data used in the study were from two sources: 1). Seismological Facility for the Advancement of Geoscience Data Management Center. The data were obtained using the BREQ\_FAST data requesting procedure (<https://ds.iris.edu/ds/nodes/dmc/forms/breqfast-request/>); and 2). China Earthquake Network Center (<https://data.earthquake.cn/index.html>). The specific data requesting parameters including the cut-off magnitude and epicentral distance range can be found in Section 2.1. The study was partially supported by the U.S. National Science Foundation under awards 1830644 and 2149587 to K.L. and 1919789 to S.G.

#### Supplementary materials

Supplementary material associated with this article can be found, in the online version, at [doi:10.1016/j.epsl.2024.118947](https://doi.org/10.1016/j.epsl.2024.118947).

#### References

- Ammon, C.J., 1991. The isolation of receiver effects from teleseismic P waveforms. *Bull. Seismolog. Soc. Am.* 81, 2504–2510.

- Bina, C.R., Helffrich, G., 1994. Phase transition Clapeyron slopes and transition zone seismic discontinuity topography. *J. Geophys. Res. Solid Earth* 99, 15853–15860. <https://doi.org/10.1029/94JB00462>.
- Clayton, R.W., Wiggins, R.A., 1976. Source shape estimation and deconvolution of teleseismic bodywaves. *Geophys. J. Int.* 47, 151–177. <https://doi.org/10.1111/j.1365-246X.1976.tb01267.x>.
- Dahm, H.H., Gao, S.S., Kong, F., Liu, K.H., 2017. Topography of the mantle transition zone discontinuities beneath Alaska and its geodynamic implications: constraints from receiver function stacking. *J. Geophys. Res. Solid Earth* 122, 10–352. <https://doi.org/10.1002/2017JB014604>.
- Dewey, J.F., Shackleton, R.M., Chang, C., Sun, Y., 1988. The tectonic evolution of the Tibetan Plateau. *Philosoph. Transact. Royal Soc. Lond. Series A, Math. Phys. Sci.* 327 (1594), 379–413. <https://doi.org/10.1098/rsta.1988.0135>.
- Ding, L., Kapp, P., Wan, X., 2005. Paleocene–Eocene record of ophiolite obduction and initial India–Asia collision, south central Tibet. *Tectonics* 24. <https://doi.org/10.1029/2004TC001729>.
- Dong, L., Li, G., Zhang, Z., 2019. Zircon U–Pb age, petrogeochemistry and Sr–Nd–Pb isotopes of the diabase in the Xuesha area, southern Tibet. *China. J. Chengdu University Techn. (Sci. Techn. Edit.)* 46, 734–745.
- Duan, Y., Tian, X., Liang, X., Li, W., Wu, C., Zhou, B., Iqbal, J., 2017. Subduction of the Indian slab into the mantle transition zone revealed by receiver functions. *Tectonophysics* 702, 61–69. <https://doi.org/10.1016/j.tecto.2017.02.025>.
- Duan, Y., Tian, X., Liu, Z., Zhu, G., Nie, S., 2016. Lithospheric detachment of India and Tibet inferred from thickening of the mantle transition zone. *J. Geodyn.* 97, 1–6. <https://doi.org/10.1016/j.jog.2016.02.001>.
- Dueker, K.G., Sheehan, A.F., 1997. Mantle discontinuity structure from midpoint stacks of converted P to S waves across the Yellowstone hotspot track. *J. Geophys. Res.* 102, 8313–8327.
- Efron, B., Tibshirani, R., 1986. Bootstrap methods for standard errors, confidence intervals, and other measures of statistical accuracy. *Statistic. Sci.* 54–75. <https://doi.org/10.1214/ss/1177013815>.
- Fei, Y., Van Orman, J., Li, J., Van Westrenen, W., Sanloup, C., Minarik, W., Funakoshi, K. I., 2004. Experimentally determined postspinel transformation boundary in Mg<sub>2</sub>SiO<sub>4</sub> using MgO as an internal pressure standard and its geophysical implications. *J. Geophys. Res. Solid Earth* 109. <https://doi.org/10.1029/2003JB002562>.
- Feng, M., An, M., Mechie, J., Zhao, W., Xue, G., Su, H., 2020. Lithospheric structures of and tectonic implications for the central–east Tibetan Plateau inferred from joint tomography of receiver functions and surface waves. *Geophys. J. Int.* 223, 1688–1707. <https://doi.org/10.1093/gji/ggaa403>.
- Gao, S.S., Liu, K.H., 2014a. Imaging mantle discontinuities using multiply-reflected P-to-S conversions. *Earth. Planet. Sci. Lett.* 402, 99–106. <https://doi.org/10.1016/j.epsl.2013.08.025>.
- Gao, S.S., Liu, K.H., 2014b. Mantle transition zone discontinuities beneath the contiguous United States. *J. Geophys. Res., Solid Earth* 119, 6452–6468. <https://doi.org/10.1002/2014JB011253>.
- Hirose, K., 2002. Phase transitions in pyrolitic mantle around 670-km depth: Implications for upwelling of plumes from the lower mantle. *J. Geophys. Res. Solid Earth* 107. <https://doi.org/10.1029/2001JB000597>. ECV-3.
- Huang, Z., Wang, P., Xu, M., Wang, L., Ding, Z., Wu, Y., Li, H., 2015. Mantle structure and dynamics beneath SE Tibet revealed by new seismic images. *Earth. Planet. Sci. Lett.* 411, 100–111. <https://doi.org/10.1016/j.epsl.2014.11.040>.
- Inoue, T., Wada, T., Sasaki, R., Yurimoto, H., 2010. Water partitioning in the Earth's mantle. *Phys. Earth Planet. Inter.* 183, 245–251. <https://doi.org/10.1016/j.pepi.2010.08.003>.
- Lei, J., Zhao, D., 2016. Teleseismic P-wave tomography and mantle dynamics beneath Eastern Tibet. *Geochem., Geophys., Geosyst.* 17, 1861–1884. <https://doi.org/10.1002/2016GC006262>.
- Lei, J., Zhao, D., Su, Y., 2009. Insight into the origin of the Tengchong intraplate volcano and seismotectonics in southwest China from local and teleseismic data. *J. Geophys. Res.* 114, B05302. <https://doi.org/10.1029/2008JB005881>.
- Lei, J., Zhao, D., Xu, X., Xu, Y.G., Du, M., 2019. Is there a big mantle wedge under eastern Tibet? *Phys. Earth Planet. Inter.* 292, 100–113. <https://doi.org/10.1016/j.pepi.2019.04.005>.
- Li, C., van der Hilst, R.D., Meltzer, A.S., Engdahl, E.R., 2008. Subduction of the Indian lithosphere beneath the Tibetan Plateau and Burma. *Earth. Planet. Sci. Lett.* 274, 157–168. <https://doi.org/10.1016/j.epsl.2008.07.016>.
- Li, C., van der Hilst, R.D., 2010. Structure of the upper mantle and transition zone beneath Southeast Asia from traveltome tomography. *J. Geophys. Res. Solid Earth* 115. <https://doi.org/10.1029/2009JB006882>.
- Li, J., Song, X., 2018. Tearing of Indian mantle lithosphere from high-resolution seismic images and its implications for lithosphere coupling in southern Tibet. *Proceed. Nat. Acad. Sci.* 115, 8296–8300. <https://doi.org/10.1073/pnas.1717258115>.
- Liang, X., Chen, Y., Tian, X., Chen, Y.J., Ni, J., Gallegos, A., Teng, J., 2016a. 3D imaging of subducting and fragmenting Indian continental lithosphere beneath southern and central Tibet using body-wave finite-frequency tomography. *Earth. Planet. Sci. Lett.* 443, 162–175. <https://doi.org/10.1016/j.epsl.2016.03.029>.
- Liang, X., Tian, X., Zhu, G., Wu, C., Duan, Y., Li, W., Teng, J., 2016b. SANDWICH: A 2D broadband seismic array in central Tibet. *Seismologic. Res. Lett.* 87, 864–873. <https://doi.org/10.1785/0220150243>.
- Litasov, K.D., Ohtani, E., Sano, A., Suzuki, A., Funakoshi, K., 2005. Wet subduction versus cold subduction. *Geophys. Res. Lett.* 32. <https://doi.org/10.1029/2005GL022921>.
- Liu, K.H., Gao, S.S., 2010. Spatial variations of crustal characteristics beneath the Hoggar swell, Algeria, revealed by systematic analyses of receiver functions from a single seismic station. *Geochem., Geophys., Geosyst.* 11. <https://doi.org/10.1029/2010GC003091>.
- Liu, K.H., Gao, S.S., Silver, P.G., Zhang, Y., 2003. Mantle layering across central South America. *J. Geophys. Res. Solid Earth* 108. <https://doi.org/10.1029/2002JB002208>.
- Liu, Z., Tian, X., Gao, R., Wang, G., Wu, Z., Zhou, B., Xu, X., 2017. New images of the crustal structure beneath eastern Tibet from a high-density seismic array. *Earth. Planet. Sci. Lett.* 480, 33–41. <https://doi.org/10.1016/j.epsl.2017.09.048>.
- Lu, C., Grand, S.P., Lai, H., Garnero, E.J., 2019. TX2019slab: A new P and S tomography model incorporating subducting slabs. *J. Geophys. Res. Solid Earth* 124, 11549–11567. <https://doi.org/10.1029/2019JB017448>.
- Mohamed, A.A., Gao, S.S., Elsheikh, A.A., Liu, K.H., Yu, Y., Fat-Helbary, R.E., 2014. Seismic imaging of mantle transition zone discontinuities beneath the northern Red Sea and adjacent areas. *Geophys. J. Int.* 199, 648–657. <https://doi.org/10.1093/gji/ggu284>.
- Murphy, M.A., Yin, A., Harrison, T.M., Durr, S.B., Ryerson, F.J., Kidd, W.S.F., 1997. Did the Indo-Asian collision alone create the Tibetan Plateau? *Geology* 25, 719–722. [https://doi.org/10.1130/0091-7613\(1997\)025<0719:DTIACA>2.3.CO;2](https://doi.org/10.1130/0091-7613(1997)025<0719:DTIACA>2.3.CO;2).
- Nie, S., Tian, X., Liang, X., Chen, Y., Xu, T., 2020. Pn uppermost mantle tomography of Central Tibet: Implication for mechanisms of NS rifts and conjugate faults. *Tectonophysics* 788, 228499. <https://doi.org/10.1016/j.tecto.2020.228499>.
- Ohtani, E., Litasov, K., Hosoya, T., Kubo, T., Kondo, T., 2004. Water transport into the deep mantle and formation of a hydrous transition zone. *Phys. Earth Planet. Inter.* 143, 255–269. <https://doi.org/10.1016/j.pepi.2003.09.015>.
- Ohtani, E., Litasov, K.D., 2006. The effect of water on mantle phase transitions. *Rev. Mineral. Geochem.* 62, 397–420. <https://doi.org/10.2138/rmg.2006.62.17>.
- Pearson, D.G., Brenker, F.E., Nestola, F., McNeill, J., Nasdala, L., Hutchison, M.T., Vince, L., 2014. Hydrous mantle transition zone indicated by ringwoodite included within diamond. *Nature* 507, 221–224. <https://doi.org/10.1038/nature13080>.
- Replumaz, A., Guillot, S., Villasenor, A., Negro, A.M., 2013. Amount of Asian lithospheric mantle subducted during the India/Asia collision. *Gondwana Res.* 24, 936–945. <https://doi.org/10.1016/j.jgr.2012.07.019>.
- Ringwood, A.E., 1975. *Composition and Petrology of the Earth's Mantle*. MacGraw-Hill, p. 618.
- Smith, W.H.F., Wessel, P., 1990. Gridding with continuous curvature splines in tension. *Geophysics* 55, 293–305. <https://doi.org/10.1190/1.1442837>.
- Smyth, J.R., 1987.  $\beta$ -Mg<sub>2</sub>SiO<sub>4</sub>: A potential host for water in the mantle? *Am. Mineral.* 72, 1051–1055.
- Smyth, J.R., Frost, D.J., 2002. The effect of water on the 410-km discontinuity: An experimental study. *Geophys. Res. Lett.* 29. <https://doi.org/10.1029/2001GL014418>, 123–1.
- Sun, M., Fu, X., Liu, K.H., Gao, S.S., 2018. Absence of thermal influence from the African Superswell and cratonic keels on the mantle transition zone beneath southern Africa: Evidence from receiver function imaging. *Earth. Planet. Sci. Lett.* 503, 108–117. <https://doi.org/10.1016/j.epsl.2018.09.012>.
- Sun, M., Gao, S.S., Liu, K.H., Fu, X., 2020. Upper mantle and mantle transition zone thermal and water content anomalies beneath NE Asia: Constraints from receiver function imaging of the 410 and 660 km discontinuities. *Earth. Planet. Sci. Lett.* 532, 116040. <https://doi.org/10.1016/j.epsl.2019.116040>.
- Thompson, A.B., 1992. Water in the Earth's upper mantle. *Nature* 358, 295–302. <https://doi.org/10.1038/358295a0>.
- Wei, W., Xu, J., Zhao, D., Shi, Y., 2012. East Asia mantle tomography: New insight into plate subduction and intraplate volcanism. *J. Asian Earth. Sci.* 60, 88–103. <https://doi.org/10.1016/j.jseaes.2012.08.001>.
- Wei, W., Xu, J., Yu, H., Wei, F., 2015. Origin of the Ashi volcano, Western Kunlun Mountains: Evidence from seismic tomography. *Earth Sci. Front.* 22, 227–232. <https://doi.org/10.13745/j.esf.2015.06.018>.
- Wei, W., Zhao, D., 2020. Intraplate volcanism and mantle dynamics of Mainland China: New constraints from shear-wave tomography. *J. Asian Earth. Sci.* 188, 104103. <https://doi.org/10.1016/j.jseaes.2019.104103>.
- Wu, C., Zuba, A.V., Chen, X., Ding, L., Levy, D.A., Liu, C., et al., 2019. Tectonics of the Eastern Kunlun Range: Cenozoic reactivation of a Paleozoic–early Mesozoic orogen. *Tectonics* 38, 1609–1650. <https://doi.org/10.1029/2018TC005370>.
- Wu, Y., Bao, X., Zhang, B., Xu, Y., Yang, W., 2022. Seismic evidence for stepwise lithospheric delamination beneath the Tibetan Plateau. *Geophys. Res. Lett.* 49, e2022GL098528. <https://doi.org/10.1029/2022GL098528>.
- Xu, J., Zhao, B., Yu, H., Wei, F., Chen, Z., 2021. Volcanic geology and petrochemistry of Ashikule volcanic field in western Kunlun Mountains of the Tibetan Plateau. *Geol. Soc.* 510. <https://doi.org/10.1144/SP510-2020-133>. London, Special Publications.
- Xu, M., Huang, H., Huang, Z., Wang, P., Wang, L., Xu, M., Yuan, X., 2018. Insight into the subducted Indian slab and origin of the Tengchong volcano in SE Tibet from receiver function analysis. *Earth. Planet. Sci. Lett.* 482, 567–579. <https://doi.org/10.1016/j.epsl.2017.11.048>.
- Yang, Y., Zhao, Z., Lei, H., Wu, J., Miao, Z., Zhang, S., Chen, L., Ji, H., 2019. Magma evolution and petrogenesis Holocene volcanic rocks in Tengchong, Yunnan. *Acta Petrologica Sinica* 35, 472–484.
- Yin, A., Harrison, T.M., 2000. Geologic evolution of the Himalayan–Tibetan orogen. *Annu Rev. Earth. Planet. Sci.* 28, 211–280. <https://doi.org/10.1146/annurev.earth.28.1.211>.
- Yu, Y., Gao, S.S., Liu, K.H., Yang, T., Xue, M., Le, K.P., 2017. Mantle transition zone discontinuities beneath the Indochina Peninsula: Implications for slab subduction and mantle upwelling. *Geophys. Res. Lett.* 44, 7159–7167. <https://doi.org/10.1002/2017GL073528>.
- Zhang, C., Dong, Y., Zhao, Y., Wu, A., Guo, K., 2003. Geochemistry of Mesoproterozoic volcanic rocks in the Western Kunlun Mountains: Evidence for plate tectonic evolution. *Acta Geologica Sinica–English Edit.* 77, 237–245. <https://doi.org/10.1111/j.1755-6724.2003.tb00567.x>.

- Zhang, F., Wu, Q., Li, Y., Zhang, R., Sun, L., Pan, J., Ding, Z., 2018. Seismic tomography of eastern Tibet: Implications for the Tibetan Plateau growth. *Tectonics*. 37, 2833–2847. <https://doi.org/10.1029/2018TC004977>.
- Zhang, H., Zhao, D., Zhao, J., Liu, H., 2015. Tomographic imaging of the underthrusting Indian slab and mantle upwelling beneath central Tibet. *Gondwana Res.* 28, 121–132. <https://doi.org/10.1016/j.gr.2014.02.012>.
- Zhang, R., Wu, Y., Gao, Z., Fu, Y.V., Sun, L., Wu, Q., Ding, Z., 2017. Upper mantle discontinuity structure beneath eastern and southeastern Tibet: New constraints on the Tengchong intraplate volcano and signatures of detached lithosphere under the western Yangtze Craton. *J. Geophys. Res. Solid Earth* 122, 1367–1380. <https://doi.org/10.1002/2016JB013551>.
- Zhao, J., Zhao, D., Zhang, H., Liu, H., Huang, Y., Cheng, H., Wang, W., 2014. P-wave tomography and dynamics of the crust and upper mantle beneath western Tibet. *Gondwana Res.* 25, 1690–1699. <https://doi.org/10.1016/j.gr.2013.06.020>.
- Zheng, H., Li, T., He, R., Yang, H., Niu, X., Zou, C., 2020. Tomographic imaging of the India-Asia plate collisional tectonics and mantle upwelling beneath western Tibet. *Acta Geologica Sinica-English Edit.* 94, 1159–1166. <https://doi.org/10.1111/1755-6724.14563>.
- Zou, H., Ma, M., Fan, Q., Xu, B., Li, S.Q., Zhao, Y., King Jr, D.T., 2017. Genesis and open-system evolution of Quaternary magmas beneath southeastern margin of Tibet: Constraints from Sr-Nd-Pb-Hf isotope systematics. *Lithos.* 272, 278–290. <https://doi.org/10.1016/j.lithos.2016.12.012>.